PAPER

Check for updates

A physical approach for the estimation of the SERS enhancement factor through the enrichment and separation of target molecules using magnetic adsorbents†

Danhui Zhao,‡[a] Kui Lin,‡[b] Lanhui Wang,[a] Zhigang Qiu, [ID][c] Xin Zhao,[d] Kunze Du,[a] Lifeng Han,[a] Fei Tian [ID] *[a] and Yanxu Chang*[a]

The controllable synthesis of nanosized Fe_3O_4 (10–20 nm) encapsulated in different numbers of graphene layers (1–5 layers) (Fe_3O_4@DGL NPs) was realized through a facile and green hydrothermal reaction at a temperature as low as 200 °C. The competitive reduction–oxidation between reducing ethylene glycol (EG) and oxidizing H_2O under hydrothermal conditions resulted in the emergence of a magnetic Fe_3O_4 core. Then, the pyrolytic reaction of the polyvinyl alcohol (PVA) molecules attached to the surface of the Fe_3O_4 core with different surface densities led to the formation of graphene with a controlled number of layers. These Fe_3O_4@DGL NPs exhibited fast adsorption and sensitive SERS detection for rhodamine B (RhB). A physical and mathematical model was proposed for the estimation of the enhancement factor (EF) by combining the adsorption efficiency and SERS of RhB. This approach and model are applicable for the adsorption, sensitive SERS detection and determination of SERS EF when using functional magnetic nanoparticles as the adsorbent. The Fe_3O_4@1G NPs were also used as a novel nano-adsorbent for the fast removal of *Escherichia coli* (*E. coli*) from an aqueous solution. The Fe_3O_4@1G NPs regenerated after 3 cycles also showed high efficiency in the adsorption and separation of RhB and *E. coli*.

Introduction

Organic pollution and the microbial contamination of water are some of the major challenges facing human society.[1] There are many kinds of organic substances and pathogens in the waste-water, which are harmful to aquatic life and drinking water sources.[2,3] Meanwhile, strenuous efforts are under way to remove these contaminants to obtain clean water or meet the discharge standard requirements.[4–6] The direct physical removal of pathogens from water through membrane filtration usually leads to high costs and low production efficiency.[7] Although the killing of pathogens in water using chemical disinfectants cuts down the costs, chemical residues increase the risk of cancer.[8] Dyestuffs are widely used in many fields, including dyeing, printing, plastic,

food, and cosmetics. It was estimated that 10–20% of dyes are directly discharged into water bodies owing to the imperfect treatment of wastewater in printing and dyeing industries. Most dyestuffs are synthetic and have complex structures; thus, it is difficult to decolorize the wastewater.[9] Rhodamine B (RhB), as a synthetic organic dye, is carcinogenic and widely used in various industrial fields. The liquid phase adsorption, enrichment, and separation of targeted pathogens and dyestuffs from water using stable and recyclable magnetic nanoadsorbents are an effective and efficient way for the low-cost and fast removal of targeted pathogens and dyestuffs from wastewater.[10]

Fe_3O_4 nanoparticles (NPs) have been intensively investigated as they possess a great deal of interesting magnetic properties, have low cost, and exhibit facile preparation.[11–13] Previous reports suggested that Fe_3O_4 NPs with sizes in the range of 10–100 nm are the most suitable for biomedical applications.[14–16] Accordingly, they have been employed in a variety of biological applications, including drug delivery,[17,18] magnetic separation and purification,[19–21] targeted therapeutics,[22–25] and clinical diagnosis.[26–28] Of particular note is that Fe_3O_4 NPs have tendencies for oxidation or etching when exposed to the air or in some specific environment,[29,30] which greatly restricts their practical applications both *in vivo* and *in vitro*.

For Fe_3O_4 NPs below the critical size (20 nm), super-paramagnetic behaviors can be shown at room temperature

[a]*Tianjin Key Laboratory of TCM Chemistry and Analysis, Tianjin University of Traditional Chinese Medicine, Tianjin, 301617, P. R. China. E-mail: tianfei.louise@163.com; tcmcyx@126.com; Tel: +86-22-5959-6163; +86-22-5959-6162*

[b]*Analytical Instrumentation Centre, Tianjin University, Tianjin 300072, P. R. China*

[c]*Department of Environment and Health, Tianjin Institute of Environmental and Operational Medicine, Tianjin 300050, P. R. China*

[d]*Key Laboratory of Pharmacology of Traditional Chinese Medical Formulae, Tianjin University of Traditional Chinese Medicine, Tianjin, P. R. China*

† Electronic supplementary information (ESI) available. See DOI: 10.1039/d0ra03019h

‡ Danhui Zhao and Kui Lin contributed equally to this work.

because of the higher thermal fluctuation energy compared with the anisotropic energy.[31–34] Fe_3O_4 NPs with small sizes are usually synthesized through a controlled coprecipitation of Fe(II) and Fe(III) ions in a basic aqueous solution.[35,36] However, two disadvantages are often mentioned in the Fe_3O_4 NPs synthesized by this approach. One disadvantage is that such small Fe_3O_4 NPs are difficult to be further modified or functionalized; another is the agglomeration during synthesis and subsequent applications. In addition, a conventional surface modification or functionalization procedure is complicated and requires drastic reaction conditions that may be highly toxic or engender environmental impact. And the surface and crystalline structure of Fe_3O_4 NPs might be damaged after chemical treatment.[14] Therefore, coating with a suitable layer is an effective approach to make up for those abovementioned disadvantages by providing the following benefits: reducing the tendency for aggregation, improving their dispersibility and stability; protecting the magnetic core from oxidation or etching; proving anchoring points for drug molecules or targeting ligands; and improving the biocompatibility and minimizing unexpected interactions.

Carbon is thought of as one of the most stable, environment-friendly, and biocompatible elements for its chemical resistance and low toxicity, as it has been applied in harsh and complicated conditions. Carbon nanomaterials, including carbon nanotubes, graphene, and carbon dots have attracted much attention for a wide variety of promising applications in biomedicine and bioimaging.[37–39]

Given the above, the carbon layers or few-layer graphene encapsulated Fe_3O_4 NPs possess better prospects in real world applications, as they combine the magnetic characteristics of Fe_3O_4 with the advantages of carbon materials. The carbon coatings or few-layer graphene may serve as barriers to protect the inner active materials, and particularly as the reaction or selective anchoring sites for the extrinsic chemical molecules.[14–22] Thus, the synthesis of Fe_3O_4 NPs with a carbon coating or few-layer graphene is of great importance in materials chemistry due to the bifunctional and controllable properties that these nanocomposites possess, as compared to their respective monofunctional counterparts. Until now, the approach to achieving carbon coated Fe_3O_4 NPs typically involved complex synthetic procedures, such as the hydrothermal synthesis of Fe_2O_3 NPs, followed by high temperature annealing or deposition of carbon layers using reductive carbon precursors.[40–44] The synthesis of Fe_3O_4 NPs coated with carbon coating and their application as anodes in lithium ion batteries have been widely reported in many reports, but there are only a few reports on the synthesis of Fe_3O_4 NPs encapsulated in graphene with a controlled number of layers and their layer-dependent magnetic properties.

We have developed a one-pot hydrothermal approach for the synthesis of nanosized spherical Fe_3O_4 (10–12 nm) coated with a single graphene layer (Fe_3O_4@1G NPs).[45] Although the Fe_3O_4@1G NPs display a narrow size distribution and long-term stability when exposed to air, the synthesis of Fe_3O_4 NPs with controlled graphene layers remains a challenge. The development of new protocols for the direct synthesis of Fe_3O_4 NPs encapsulated in graphene with a controlled number of layers is

quite important and interesting from a fundamental science perspective, and for application in highly selective adsorption and extraction, sensitive SERS detection, advanced drug delivery and therapeutic systems.

In this work, we further developed a well-designed strategy for the synthesis of Fe_3O_4 NPs encapsulated in few-layer graphene through a hydrothermal reaction without the subsequent high temperature annealing or coating treatment for the growth of carbon or graphene layers. The formation of the layers was attributed to the dehydration reaction of polyvinyl alcohol (PVA), and the number of the layers was dependent on the quantity of PVA molecules attached to the surface of the Fe_3O_4 NPs. The number of layers can be changed from 1 to 5 by simply altering the ratio of H_2O/EG in the solution. The as-prepared Fe_3O_4@DGL products were then readily separated using an external magnet and purified in the laboratory by alternatively using water and ethanol, which reduced environmental issues owing to the ease of operation and high yield. The presence of the layers not only endowed the Fe_3O_4@DGL NPs with stability, low toxicity, and biocompatibility, but also empowered them with superior adsorption capacity for specific molecules or bacteria. The as-purified Fe_3O_4@1G NPs displayed excellent adsorption toward rhodamine B (RhB) molecules, and could be easily separated from solution for following SERS detection with sensitivity and specificity. A physical model was established for a reasonable evaluation on the SERS enhancement factor. Based on the model and literature, a simple formula was further deduced for the calculation of EF. The calculation results show that EF is as high as 2.2×10^5 for RhB from the Fe_3O_4@1G NPs. The approach and model can be extended to other functional magnetic nanoparticles as an adsorbent for the adsorption, separation, SERS detection and determination of EF. Moreover, the Fe_3O_4@1G NPs showed highly effective adsorptive removal behavior in water solution. To the best of our knowledge, this facile and scalable synthesis of Fe_3O_4@DGL with a size-controllable Fe_3O_4 core (in the range of 10–20 nm) and graphene with a controlled number of layers (1–5 layers) has not been reported. The stable layers are suitable for further versatile functionalization for constructing highly selective and sensitive SERS-based molecular sensing arrays or developing an effective nano-adsorbent for bacteria in the future.

Materials and methods

Chemicals and materials

Polyvinyl alcohol (PVA), iron(III) nitrate enneahydrate ($Fe(NO_3)_3 \cdot 9H_2O$), ethylene glycol (EG), and rhodamine B (RhB) were purchased from Sigma-Aldrich Co. All chemicals were of analytical grade and used as received without further purification. Ultrapure fresh water prepared from a Millipore water purification system was used throughout the experiments.

Preparation and purification of Fe_3O_4@DGL

Fe_3O_4@DGL was successfully synthesized based on the strategy shown in Scheme 1. The synthesis process for Fe_3O_4@DGL consists of two steps. The first step involves the preparation of the starting solution containing $Fe(NO_3)_3 \cdot 9H_2O$, H_2O and EG.
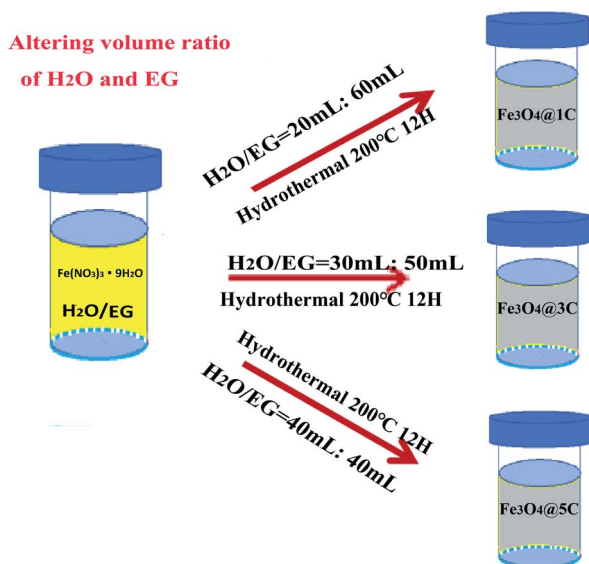
Scheme 1 Schematic illustration for the synthesis of Fe_3O_4@DGL products.

The second step is the hydrothermal treatment of the starting solution at 200 °C for 12 h. Representative Fe_3O_4 NPs with particle sizes in the range of 10–12 nm coated with a single layer graphene (Fe_3O_4@1G) were synthesized and purified, as described in our previous work.[45]

By applying the same precursors and maintaining the same total volume of 80 mL, the size of the Fe_3O_4 core and number of graphene layers was readily tuned by changing the volumetric ratio of H_2O and EG between 1 : 4 and 1 : 1. Generally, the 3 layers of graphene (Fe_3O_4@3G) and 5 layers (Fe_3O_4@5G) encapsulated Fe_3O_4 NPs were successfully synthesized using 30 mL H_2O/50 mL EG, 40 mL H_2O/40 mL EG, respectively. The as-synthesized Fe_3O_4@3G and Fe_3O_4@5G was separated and purified following the same procedures for Fe_3O_4@1G. It should be mentioned that the yield of the Fe_3O_4@DGL products gradually decreased with increasing H_2O/EG volume ratio.

SERS detection of RhB using Fe_3O_4@DGL as a substrate

As an effective and easily available bio-indicator, RhB was used as a target molecule for the evaluation of SERS activity of Fe_3O_4@1G NPs.[45] In this work, the SERS activity of Fe_3O_4@DGL NPs was further investigated using RhB as the probe molecule. The purified and freeze-dried Fe_3O_4@DGL NPs were directly put into an aqueous solution of RhB with a concentration of 10^{-5} mol L^{-1}, and followed by ultrasonic treatment for 10 min to realize RhB molecule adsorption. Then, the Fe_3O_4@DGL NPs were extracted using a strong magnet outside the bottom of the beaker. Finally, the extracted Fe_3O_4@DGL NPs with RhB molecules were dried in the open air at room temperature and used for SERS measurement.

Adsorption behaviors of RhB on Fe_3O_4@1G NPs

In order to investigate the adsorption capacity of Fe_3O_4@1G NPs on RhB, the calibration curve of the RhB solution was obtained by acquiring the absorbance value at 554 nm. In detail,

15 mg L^{-1} RhB solution was prepared by adding 1.5 mg RhB into 100 mL deionized water. Then, RhB working solutions with different concentrations were freshly prepared by serial dilution with deionized water, including 1, 2, 4, 4.8, 6, 8, 10, 12, and 15 mg L^{-1}. The amount of RhB adsorbed was calculated from the difference between its concentration before and after adsorption using Fe_3O_4@1G NPs as the adsorbent.

10^{-5} mol L^{-1} (~4.8 mg L^{-1}) RhB working solution was used to evaluate the adsorption capacities of Fe_3O_4@1G NPs. The adsorption process was performed in a 5 mL container, which contained 3 mL of RhB solution. Different amounts (5–200 mg) of Fe_3O_4@1G NPs were added to the RhB solution, and agitated at 240 rpm for 10 min at room temperature condition. Then, all solutions were vortexed for 5 min in dark conditions and the mixture were centrifuged at 900 rpm for 10 min. The concentrations of the remaining RhB solutions were determined by monitoring the absorbance at the maximum wavelength (554 nm) with a UV-Vis spectrophotometer. The adsorption efficiency was calculated according to eqn (1), as follows:

$$\% \text{ Absorption} = \frac{C_0 - C_q}{C_0} \times 100 \tag{1}$$

where C_0 and C_q are the initial and remnant concentrations of the RhB solution, respectively.

Removal of *E. coli* using Fe_3O_4@1G NPs as an adsorbent

The removal experiments of *E. coli* were performed according to the procedures and methods reported by Abdolmaleki *et al.*[46] The Gram-negative *E. coli* were inoculated into Luria–Bertani (LB) media containing 5 g L^{-1} of yeast extract, 10 g L^{-1} of bacto tryptone, and 5 g L^{-1} of NaCl, and grown at 37 °C overnight with agitation. Then, the bacteria were harvested by centrifugation at 6000 rpm for 10 min, washed 2 times with phosphate buffered solution (PBS, pH 7.4), and resuspended in PBS to derive a bacterial stock solution with an OD_{600} value of about 0.1 at a density of 10^8 CFU mL^{-1}. Then, different amounts of Fe_3O_4@1G NPs (0.05, 0.1, 0.2 g) were added to 10 mL of microbial suspension. All bacterial suspensions were incubated and agitated at 240 rpm for 10 min. Finally, the Fe_3O_4@1G NPs were separated from the suspension using a strong magnet outside the bottom of the vial. The supernatant containing residual bacteria was put way for further investigation. All microbial suspensions of *E. coli* were gradient-diluted and the live bacteria numbers were determined by counting the numbers of CFU on solid LB agar plates. Initial bacterial concentration was determined to be 2.28×10^8 CFU_0 mL^{-1}. The removal efficiency for different amounts of the as-purified Fe_3O_4@1G NPs was calculated by the following expression:

$$\text{Removal efficiency } (100\%) = \frac{CFU_0 - CFU_t}{CFU_0} \times 100\%$$

where CFU_0 and CFU_t are the initial and residual numbers of bacterial colonies in the samples.

Recyclability of the Fe_3O_4@1G NPs

To evaluate the recyclability of the Fe_3O_4@1G NPs, 200 mg of used nano-adsorbent was repeatedly washed with methanol

solution (50%, v/v) 3 times, and then dried in a vacuum oven at 80 °C for 2 h. Then, the regenerated Fe_3O_4@1G NPs was used for the next adsorption of RhB or removal of *E. coli*.

Characterizations

The phase of the Fe_3O_4@DGL products were investigated using a Rigaku D/max 2500v/pc XRD. Transmission electron microscopy (TEM) was conducted on an FEI Tecnai G2 F20 with a field emission gun to examine the morphology and structure of the Fe_3O_4@DGL products. The composition was analyzed using an energy dispersive X-ray spectrometer (EDS) purchased from EDXA, Inc. Raman spectroscopy was performed using a Renishaw inVia Reflex confocal Raman microscope with a 633 nm laser with the power set to 20 mW. The magnetic properties of the samples were recorded with a Squid-VSM Magnetic Measuring System (Squid-VSM). UV-Vis absorption was performed on an Agilent UV/Vis/NIR spectrophotometer. The initial and residual numbers of the bacterial colonies in the samples were roughly assessed after 24 hours of incubation by measuring the optical density (OD) value at 595 nm and 620 nm using a TECAN Infinite 200 PRO Nanoquant (Tecan Instruments, Switzerland).

Results and discussion

The morphology, size and crystalline structure of all Fe_3O_4@-DGL products were examined with TEM, XRD and Raman

spectroscopy. Fig. 1 shows the TEM images of Fe_3O_4@DGL with different sizes and graphene layers. All Fe_3O_4@DGL NPs display a uniform spherical core–shell structure with ultrathin graphene layers as marked by white arrows in Fig. 1b, d and f, and the average size of the Fe_3O_4@DGL NPs was estimated to be in the range of 10–20 nm (Fig. S1†).

A low-magnification TEM image in Fig. 1a shows that the Fe_3O_4@1G NPs had uniform spherical with a very narrow size distribution of 10–12 nm (Fig. S1a†), but appeared mostly connected to each other. More detailed structural analysis of Fe_3O_4@1G NPs by high resolution TEM (HRTEM) in Fig. 1b reveals that the Fe_3O_4 core was coated with one single graphene layer. The inner Fe_3O_4 core was an intact crystal grain with a size in the range of 10–12 nm and coated with a single layer graphene. As can be seen, the outer graphene layer was uniform and continuous, which were believed to provide reliable and effective protection for the Fe_3O_4 core from directly etching or oxidized as served in harsh environments.

The size of the Fe_3O_4 core and number of graphene layers were easily controlled by changing the ratio of H_2O/EG for the dissolution of the starting precursors. As shown in Fig. 1c and d, the size of the Fe_3O_4 core in the Fe_3O_4@3G products was in the range of 12–16 nm (Fig. S1b†) and encapsulated in 3 layers graphene. The inner core also consisted of a single crystal Fe_3O_4 nanoparticle. For Fe_3O_4@5G, the size of the Fe_3O_4 core was in the range of 16–20 nm (Fig. S1c†) and encapsulated in 5 layers of graphene, as shown in Fig. 1e and f. However, the core was not actually composed of a single nanocrystal. The basic structures in the core are obscure and not easily identified.

In order to identify the crystalline structure and graphitic quality of the graphene layer, all three Fe_3O_4@DGL products were further evaluated by XRD and Raman spectroscopy. As shown in Fig. 2a, the XRD patterns of all three products exhibited typical (220), (311), (400), (422), (511) and (440) diffraction peaks indexed to Fe_3O_4 (JCPDS file no. 75-1609). Interestingly, all XRD patterns showed a weak diffraction peak at around $2\theta = 24°$ with an index of (002) resulting from the ordered carbon atoms outside the Fe_3O_4 core. The average single crystal size of the Fe_3O_4 NPs calculated by the Scherrer equation was about 11 nm, 15 nm and 18 nm, respectively, which agreed well with the sizes estimated from TEM. Furthermore, the strong and broad diffraction peaks indicated the well-crystallized characteristic of the Fe_3O_4 core. The interplanar distance was measured to be 0.252 nm or 0.492 nm
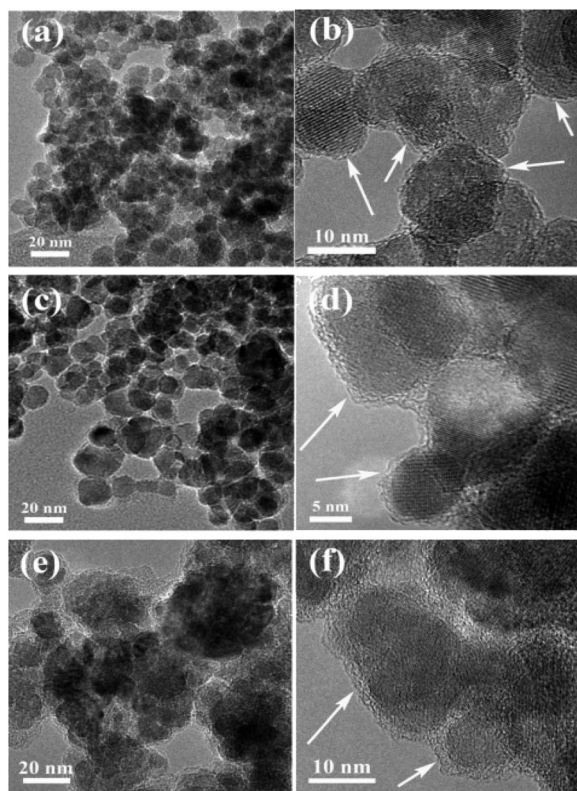

Fig. 1 (a) Low magnification and (b) corresponding high-resolution TEM images of the Fe_3O_4@1G NPs; (c) and (d) Fe_3O_4@3G NPs; (e) and (f) Fe_3O_4@5G NPs.
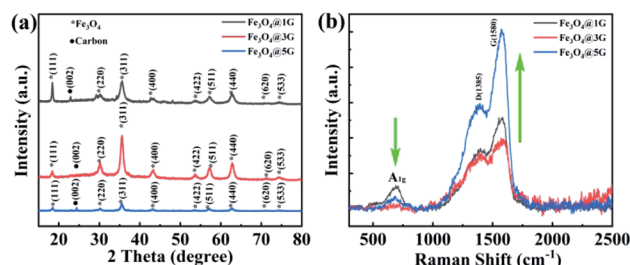

Fig. 2 (a) XRD patterns and (b) Raman spectra of the Fe_3O_4@DGL products.

(Fig. S2†), which corresponded to the (311) or (111) spacing of Fe_3O_4. The corresponding selected area electron diffraction (SAED) pattern in Fig. S3† implied the polycrystalline features of the as-obtained Fe_3O_4@DGL products, and the diffraction ring was ascribed to the {111}, {220}, {311}, {222}, {440}, {422} planes of the cubic Fe_3O_4. In addition, the quantitative EDS result shown in Fig. S4† revealed that Fe_3O_4@DGL was only composed of C, Fe and O.

The Raman spectrum was collected in the range of 400–2500 cm^{-1}, corresponding to the spectral region that provides the most valuable data on the lattice-vibration modes of Fe_3O_4 and structural properties of carbon materials. Three broad bands were clearly identified in the Raman spectrum of three Fe_3O_4@DGL products, as shown in Fig. 2b. The Raman bands at 698 cm^{-1} were designated as A_{1g} mode, which refers to the symmetric stretch of oxygen atoms along Fe–O bonds.[47,48] The other two bands centered at about 1390 cm^{-1} and 1580 cm^{-1} corresponded to the D band and G band of carbon materials, respectively. The broadening and downshifting of the Raman feature peak at 1390 cm^{-1} of the Fe_3O_4@DGL products also indicated that the outer layer was nano-scale. The peak intensity ratio between the D- and G-bands (I_D/I_G) correlates with the degree of crystallinity of the carbon materials. The smaller ratio of I_D/I_G, the higher the degree of crystallinity in the carbon material.[40,41] The I_D/I_G ratios for the Fe_3O_4@1G, Fe_3O_4@3G, Fe_3O_4@5G samples were calculated to be 0.61, 0.60, and 0.64, respectively, which were smaller than that of graphene[49] and other carbon coated Fe_3O_4 NPs,[40,41] demonstrating a high degree of crystallinity of carbon in all three samples. It is worth noting that the relative intensity of the A_{1g} mode with respect to the D-band/G-band decreased with increasing size of the Fe_3O_4 core and number of graphene layers due to the shielding effect from the outer layers. The chemically inert carbon coating or graphene layers might be the ideal anchoring or attaching sites for the target molecules. The variation of relative intensities in the Raman spectra also suggests that Fe_3O_4 with different sizes and graphene layers could lead to various interface polarization and complex relaxations, which is quite important for the ultrasensitive detection of trace quantities of target molecules through surface-enhanced Raman spectroscopy (SERS).[50–52]

All of the above results indicated that the as-obtained products were pure Fe_3O_4@DGL NPs with a size-controllable Fe_3O_4 core and tunable graphene layers. The uniform spherical Fe_3O_4@DGL NPs were synthesized using the modified procedure and recipe *via* a facile and green hydrothermal process.

The magnetization curves measured at 300 K are shown in Fig. 3. The magnetic properties determined by SQUID-VSM at 300 K revealed magnetization saturation values of 79.8, 60.3 and 30.7 emu g^{-1} for Fe_3O_4@1G, Fe_3O_4@3G, and Fe_3O_4@5G, respectively, with no remanence and coercivity hysteresis, indicating the superparamagnetic property of the as-obtained Fe_3O_4@DGL NPs. The magnetic saturation values of all three Fe_3O_4@DGL products were smaller than that of the bulk material (92 emu g^{-1}) and single-crystalline Fe_3O_4 with diameters of 200 nm (81.9 emu g^{-1}). The magnetization saturation values showed a decrease with increasing Fe_3O_4 core size and graphene layers, mainly attributed to the decrease in the degree

of crystallinity of Fe_3O_4 and partly to the diamagnetic shielding effect from the graphene layers. Similar to other magnetic core–shell nanostructures, the magnetic saturation values also had a large dependence on the size of the Fe_3O_4 core and thickness of the carbon coating.[53,54]

PVA is a water-soluble synthetic polymer and has the idealized linear molecular structure. The PVA molecules have been successfully used for the construction of a relative pure and clean surface due to their stability at low temperatures and abundant OH groups.[55]

Generally, the formation process of the Fe_3O_4@1G NPs can be briefly described as the following three sequential stages (from our previous report).[45] (1) Fe_3O_4 NPs with abundant –OH groups were first formed arising from the reaction between Fe^{3+} and reducing agent EG under hydrothermal conditions. (2) The well-ordered alignment of the PVA molecular chains on the surface of the Fe_3O_4 NPs was attributed to the combination between the –OH groups from the PVA molecules and the surfaces of the Fe_3O_4 NPs. (3) A subsequent dehydration reaction resulted in the formation of the graphene layer grown on the surface of the Fe_3O_4 NPs. It should be noted that a good amount of PVA molecules conjugated with the –OH on the surface of Fe_3O_4 would result in the formation of a relatively pure and clean graphene layer from such simple dehydration reaction, but more PVA molecules lead to the formation of corrugated or stacked multiple layers of graphene due to more intermolecular or intramolecular dehydration reactions in the PVA molecules.

For the Fe_3O_4@DGL NPs with different core sizes and graphene with a controlled number of layers, the formation mechanism of Fe_3O_4@DGL was further proposed and described as follows. EG is a widely used chemical for the preparation of Fe_3O_4 NPs by virtue of its reducibility at high temperatures.[56–58] The H_2O molecule also has a strong oxidization at high temperature.[59] Under hydrothermal conditions, all precursors and solvents endured high temperature and high pressure in an autoclave with a confined space. Thus, not only the reduction of Fe^{3+} into Fe^{2+} was tuned by the dynamic reduction–oxidation between EG and H_2O, but also the graphene layer could be regulated due to the intermolecular and/or intramolecular dehydration of PVA attached to the surface of the Fe_3O_4 NPs by altering the ratio of EG/H_2O. As many researchers have noted, small magnetic Fe_3O_4 NPs with –OH groups were first formed resulting from the reduction of EG, but have a tendency to form large agglomerates during the initial stage of the hydrothermal reaction.[44,45] With the increasing of the ratio between H_2O and EG, we believe that a larger Fe_3O_4 core could be formed due to the intensive oxidation–reduction competition between the oxidizing ionized –OH groups from H_2O and reductant EG with low concentration in the solution. Iron is a key limiting resource in this reaction system. A greater amount of –OH groups from H_2O renders a larger size of Fe_2O_3 NPs, but the reductive EG is responsible for the transformation of the Fe_2O_3 NPs into Fe_3O_4 NPs. This also explained why the higher H_2O/EG ratio did not produce the Fe_3O_4@C nanoparticles, but the formation of red Fe_2O_3 NPs. The attached PVA molecules on the surface of the Fe_3O_4 core underwent a dehydration reaction, leading to the
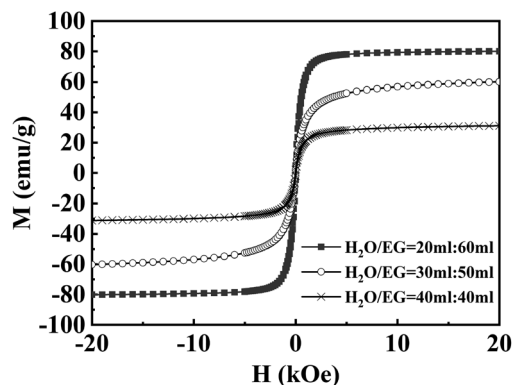
Fig. 3 Magnetization curves of the three Fe_3O_4@DGL products obtained at 300 K.

presence of graphene layers. What is different from the formation of Fe_3O_4@1G in the second stage is that the density of the hydrophilic –OH groups on the surface of the Fe_3O_4 core also increased as a result of a great deal of ionized –OH from H_2O at high temperature. Therefore, the amount of PVA molecules attached to the surface of the Fe_3O_4 core was significantly improved, which in turn determined the number of graphene layers coated on the Fe_3O_4 core in the following dehydration reaction, as illustrated in Fig. S5.† As more H_2O was introduced into the system, i.e., H_2O/EG ratio of 60 : 20 mL, the color of the starting solution changed from yellow to brown after the identical hydrothermal treatment. The obtained product was identified as being a mixture of Fe_2O_3 and Fe_3O_4 NPs (Fig. S6†), and the cores were coated with about 3 graphene layers, as confirmed by TEM (Fig. S7†). The formation of the mixture of Fe_2O_3 and Fe_3O_4 NPs might be ascribed to an oxidizing environment arising in the autoclave.

PVA, rich in OH groups, was used as a precursor and was responsible for the presence of different graphene layers through a dehydration reaction under hydrothermal conditions. The theoretical prediction and experimental results demonstrated that atom-thick graphene layers effectively improved the adsorption capacity on the organic molecules with aromatic rings due to a structural similarity, and remarkably enhanced the Raman signal and minimized the back action noise.[60–63] The Raman spectra in Fig. 5 showed that the

Fe_3O_4@1G NPs displayed the strongest enhancement ability of SERS toward RhB.

Fig. 4 shows the SERS spectrum of RhB with different concentrations adsorbed on the Fe_3O_4@1G substrate and 10^{-3} mol L^{-1} RhB adsorbed on Fe_3O_4@DGL NPs. The typical vibrational characteristic peaks of RhB were clearly identified for all SERS spectra and agreed well with the published literature.[64] As seen in Fig. 4a, the SERS spectrum of RhB adsorbed on Fe_3O_4@1G exhibits both concentration-dependent properties and six very sharp distinct characteristic peaks, indicating a high signal-to-noise ratio. In detail, the peaks at 1280, 1355, 1507, and 1645 cm^{-1} are attributed to the C–C stretching vibration in the aromatic ring. The peaks at 1192 cm^{-1} arise from the C–H in-plane bending vibration. The peak at 627 cm^{-1} is ascribed to the in-plane C–C–C stretching vibration in the aromatic ring. It should be noted that the visible characteristic peak that appeared at 1280 cm^{-1} can be regarded as a distinguishing feature of RhB that differentiates it from rhodamine 6G (R6G).[63] Raman spectra of RhB adsorbed on Fe_3O_4@3G and Fe_3O_4@5G substrates were also performed to investigate the influence of the size and graphene layers of Fe_3O_4@DGL. The SERS spectra of RhB adsorbed on three Fe_3O_4@DGL substrates shared the similar characteristic peaks as shown in Fig. 4b, implying that all Fe_3O_4@DGL substrates are SERS active, but the Fe_3O_4@1G substrates had more remarkable SERS enhancement activities compared to the other two substrates. With increasing size and number of graphene layers, the SERS enhancement effect decreased.

The SERS enhancement factor (EF) is particularly important for the practical application of the substrates. The SERS enhancement factor, EF, is expressed as:[64–67]

$$EF = (I_{SERS}/I_{Bulk}) \times (N_{Bulk}/N_{Surf}) \quad (2)$$

where I_{SERS} and I_{Bulk} are the vibration intensities in the SERS and normal Raman spectra of RhB, respectively. N_{Bulk} and N_{Surf} are the number of molecules under laser illumination for the bulk sample, and the number of molecules adsorbed on the surface of Fe_3O_4@1G NPs, respectively.

Fig. 5 illustrates the in situ SERS detection of RhB using Fe_3O_4@1G NPs as the substrate and the ideal area and penetration depth profile under laser illumination for the estimation of the number of RhB molecules adsorbed on the Fe_3O_4@1G NPs in the bulk sample.
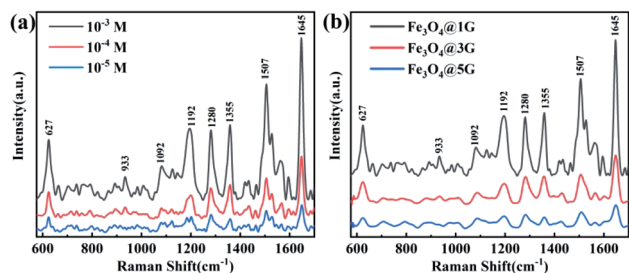

Fig. 4 (a) SERS spectra of 10^{-3}, 10^{-4} and 10^{-5} mol L^{-1} RhB adsorbed on Fe_3O_4@1G NPs. (b) SERS spectra of 10^{-3} mol L^{-1} RhB adsorbed on Fe_3O_4@1G, Fe_3O_4@3G, and Fe_3O_4@5G, respectively.
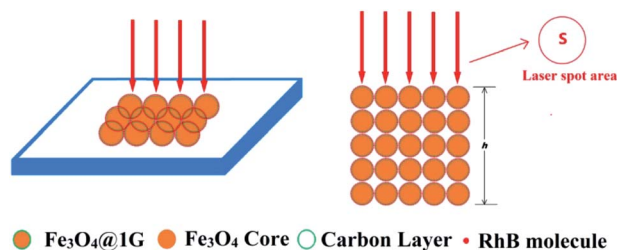

Fig. 5 Schematic illustration of (a) in situ SERS detection of RhB adsorbed on the Fe_3O_4@1G NPs, and (b) ideally illuminated area and penetration depth profile of the laser spot for the estimation of the number of RhB molecules in the bulk sample.

For the estimation of the illuminated volume of RhB molecules or RhB molecules adsorbed on $Fe_3O_4@1G$ NPs, a simplified circular column was introduced to describe the corresponding sampling area and the penetration depth of the RhB molecules under laser illumination.

The N_{Surf} and N_{Bulk} values were calculated based on the number density of the RhB molecules adsorbed on the $Fe_3O_4@1G$ NPs, the number density of the bulk RhB, respectively. According to the measured adsorption capacity of the $Fe_3O_4@1G$ NPs, the approximate number density of the RhB molecules adsorbed on the $Fe_3O_4@1G$ NPs could be estimated by

$$n_{Surf} = \frac{\left(\frac{q_e \times V}{m_0}\right) \times N_A}{\left(\frac{M_1}{\rho_0}\right)} \quad (3)$$

where q_e, V and m_0 are the equilibrium adsorption capacity of RhB on $Fe_3O_4@1G$ NPs, volume of the solution, and molecular weight of RhB, respectively. N_A is the Avogadro constant, M_1 is the weight of the adsorbent $Fe_3O_4@1G$ NPs in the solution, and ρ_0 is the estimated density of the $Fe_3O_4@1G$ NPs.

The number density of the bulk RhB molecules can be calculated by the following equation:

$$n_{Bulk} = \frac{\rho_R}{m_0} \times N_A \quad (4)$$

where ρ_R is the density of the bulk RhB, m_0 is the molecular weight of RhB, and N_A is the Avogadro constant.

For taking the sampling area and penetration depth into account, the number of RhB molecules adsorbed on the $Fe_3O_4@1G$ NPs under laser illumination could be determined by:

$$N_{Surf} = n_{Surf} \times S \times h \quad (5)$$

where S is the area of the focused laser spot, and h is the penetration depth of the focused laser beam.

For the bulk RhB, the number of RhB molecules under laser illumination is expressed as:

$$N_{Bulk} = n_{Bulk} \times S \times h \quad (6)$$

Theoretically, the penetration depth of the focused laser beam for the SERS sampling is smaller than that for the bulk sampling due to the closely packed structure of Fe_3O_4.

Here, we assume that the SERS sampling and bulk sampling share an identical area of laser spot and penetration depth.

Substituting the values of those variables into eqn (2), the EF was calculated to be as high as 2.2×10^5 and 1.64×10^5 for RhB with a concentration of 10^{-5} mol L^{-1} from the $Fe_3O_4@1G$ NPs for the bands at 1507 cm^{-1} and 1645 cm^{-1}, respectively.

Therefore, we believe that the SERS enhancement of the $Fe_3O_4@1G$ substrates toward RhB molecules can be attributed to the uniform and continuous single graphene layer on the surface of the nanosized Fe_3O_4 NPs. The SERS enhancement in the $Fe_3O_4@1G$ substrates could be attributed to the chemical and electromagnetic effects, as described by Chen *et al.*[63] These

Table 1 Removal rate for *E. coli* bacteria with a concentration of 10^8 CFU mL^{-1} by different weights of $Fe_3O_4@1G$ NPs

Adsorbent	Weight (g)	Removal rate (%)
$Fe_3O_4@1G$ NPs	0.05	16.01
	0.1	70.39
	0.2	91.78

core–shell magnetic $Fe_3O_4@DGL$ NPs are expected to be used for the *in situ* adsorption and detection of organic dye pollutants in aqueous solution, separation and enrichment of active ingredients from natural medicine and other fields.

The calibration curve of a series of RhB working solution is shown in Fig. S8.† The effect of different amounts of $Fe_3O_4@1G$ NPs on the removal of RhB from water with a concentration of 4.8 mg L^{-1} was further investigated, and is shown in Fig. S9.† The result showed that the percent removal of RhB increased with increasing amount of nano-adsorbent $Fe_3O_4@1G$ NPs, and reached the maximum removal efficiency of 90% when the concentration of $Fe_3O_4@1G$ NPs reached about 72 mmol. This tendency may be attributed to the fact that increasing the $Fe_3O_4@1G$ NPs led to an increase of more interaction sites for the adsorption of RhB molecules, but finally stabilizes due to the adsorption equilibrium of RhB molecules in the solution.

Because of their excellent adsorption capacity and separation performance on RhB, implying the possible interaction between surface groups and with bacteria, $Fe_3O_4@1G$ NPs were also used to remove *E. coli* bacteria from an aqueous solution.

As shown in Table 1, increasing the amount of $Fe_3O_4@1G$ NPs led to an increase in the removal rate for *E. coli*. The tendency could be attributed to the presence of more interaction sites from adding more $Fe_3O_4@1G$ NPs. For 0.2 g of $Fe_3O_4@1G$ NPs, the removal rate for the *E. coli* bacteria was as high as 91%. This result showed that the $Fe_3O_4@1G$ NPs could be used for the removal of bacterial contamination. The existence of functional groups on the surface of $Fe_3O_4@1G$ NPs (including hydroxyl and carboxyl groups) renders the excellent adsorption performance towards bacteria or dye molecules.

The regenerated $Fe_3O_4@1G$ NPs still showed good adsorption efficiency for RhB and removal rate for *E. coli* from water after 3 cycles (Fig. S10†). The adsorption or removal performance was almost unchanged in the first 3 reuse cycles, which could be attributed to the recovery of the surface groups and super stability of the graphene layer. Because of its impressive adsorption and separation performance, long-term stability in the open air/operating environment, as well as excellent reusability, the synthesized $Fe_3O_4@1G$ NPs also have potential applications in wastewater treatment.

This new ability to synthesize $Fe_3O_4@DGL$ is not only beneficial in terms of the surface chemistry and understanding the dehydration reaction under hydrothermal conditions, but also provides new opportunities for the application of $Fe_3O_4@DGL$ in SERS or the efficient extraction/loading of active compounds. One possible application for $Fe_3O_4@1G$ NPs is the separation and SERS detection of targeted molecules due to the

narrow size distribution of the Fe_3O_4 core, and outer continuous and uniform single layer graphene. Another potential application of the Fe_3O_4@1G NPs is a novel magnetic nanoadsorbent for the highly effective removal of bacteria from an aqueous solution. Owing to the biocompatibility and chemically inert property of the carbon layer, the further functionalization of Fe_3O_4@DGL is expected to provide more versatility in the future.

Conclusions

In summary, a facile and green synthesis approach has been developed to prepare core–shell Fe_3O_4@DGL NPs with a controllable diameter Fe_3O_4 core and graphene with a controlled number of layers *via* a competitive oxidation–reduction under hydrothermal conditions. Uniform and well-dispersed Fe_3O_4@DGL NPs were separated and purified easily from the as-synthesized mixture in the presence of an external magnetic field. The magnetization saturation values of the Fe_3O_4@DGL NPs displayed size- and thickness-dependent characteristics. The formation mechanism of the magnetic Fe_3O_4@DGL NPs was described in detail at the molecular level. This work provides one new perspective for the green synthesis of Fe_3O_4@DGL NPs, which will minimize the use of harsh chemicals and generation of chemical waste. The stable and uniform Fe_3O_4@1G NPs may be used as a SERS substrate for the highly selective and sensitive detection of some compounds. The interaction sites on the Fe_3O_4@1G NPs may also serve as nano-adsorbents for the physical removal of bacteria during water treatment.

Conflicts of interest

The authors declare no competing financial interests.

Acknowledgements

Notes and references

1 J. A. Mazumder, M. Perwez, R. Noori and M. Sardar, Development of sustainable and reusable silver nanoparticle-coated glass for the treatment of contaminated water, *Environ. Sci. Pollut. Res.*, 2019, **26**, 23070–23081.

2 A. Hata, M. Inaba, H. Katayama and H. Furumai, Characterization of Natural Organic Substances Potentially Hindering RT-PCR-Based Virus Detection in Large Volumes of Environmental Water, *Environ. Sci. Technol.*, 2017, **51**, 13568–13579.

3 S. Arora, A. Rajpal and A. A. Kazmi, Antimicrobial Activity of Bacterial Community for Removal of Pathogens during Vermifiltration, *J. Environ. Eng.*, 2016, **142**, 04016012.

4 T. Y. Liu, C. L. Chen, Y. C. Lee, T. Y. Chan, Y. L. Wang and J. J. Lin, First Observation of Physically Capturing and Maneuvering Bacteria using Magnetic Clays, *ACS Appl. Mater. Interfaces*, 2016, **8**, 411–418.

5 V. Jegatheesan, B. K. Pramanik, J. Chen, D. Navaratna, C. Y. Chang and L. Shu, Treatment of textile wastewater with membrane bioreactor: a critical review, *Bioresour. Technol.*, 2016, **204**, 202–212.

6 C. X. H. Su, L. W. Low, T. T. Teng and Y. S. Wong, Combination and hybridisation of treatments in dye wastewater treatment: a review, *J. Environ. Chem. Eng.*, 2016, **4**, 3618–3631.

7 C. Liu, X. Xie, W. Zhao, N. Liu, P. A. Maraccini, L. M. Sassoubre, A. B. Boehm and Y. Cui, Conducting nanosponge electroporation for affordable and high-efficiency disinfection of bacteria and viruses in water, *Nano Lett.*, 2013, **13**, 4288–4293.

8 X. F. Li and W. A. Mitch, Drinking Water Disinfection Byproducts (DBPs) and Human Health Effects: Multidisciplinary Challenges and Opportunities, *Environ. Sci. Technol.*, 2018, **52**, 1681–1689.

9 C. R. Holkar, A. J. Jadhav, D. V. Pinjari, N. M. Mahamuni and A. B. Pandit, A critical review on textile wastewater treatments: possible approaches, *J. Environ. Manage.*, 2016, **182**, 351–366.

10 P. C. Pinheiro, A. L. Daniel-da-Silva, H. I. S. Nogueira and T. Trindade, Functionalized Inorganic Nanoparticles for Magnetic Separation and SERS Detection of Water Pollutants, *Eur. J. Inorg. Chem.*, 2018, 3443–3461.

11 R. A. Revia and M. Zhang, Magnetite nanoparticles for cancer diagnosis, treatment, and treatment monitoring: recent advances, *Mater. Today*, 2016, **19**, 157–168.

12 Y. Liu, Y. Fu, L. Liu, W. Li, J. Guan and G. Tong, Low-Cost Carbothermal Reduction Preparation of Monodisperse Fe_3O_4/C Core-Shell Nanosheets for Improved Microwave Absorption, *ACS Appl. Mater. Interfaces*, 2018, **10**, 16511–16520.

13 D. Ling, N. Lee and T. Hyeon, Chemical synthesis and assembly of uniformly sized iron oxide nanoparticles for medical applications, *Acc. Chem. Res.*, 2015, **48**, 1276–1285.

14 Wahajuddin and S. Arora, Superparamagnetic iron oxide nanoparticles: magnetic nanoplatforms as drug carriers, *Int. J. Nanomed.*, 2012, 7, 3445–3471.

15 C. Blanco-Andujar, A. Walter, G. Cotin, C. Bordeianu, D. Mertz, D. Felder-Flesch and S. Begin-Colin, Design of iron oxide-based nanoparticles for MRI and magnetic hyperthermia, *Nanomedicine*, 2016, **11**, 1889–1910.

16 A. Hofmann, S. Thierbach, A. Semisch, A. Hartwig, M. Taupitz, E. Rühl and C. Graf, Highly monodisperse water-dispersable iron oxide nanoparticles for biomedical applications, *J. Mater. Chem.*, 2010, **20**, 7842–7853.

17 L. H. Reddy, J. L. Arias, J. Nicolas and P. Couvreur, Magnetic nanoparticles: design and characterization, toxicity and

biocompatibility, pharmaceutical and biomedical applications, *Chem. Rev.*, 2012, **112**, 5818–5878.

18 A. Hervault and N. T. K. Thanh, Magnetic nanoparticle-based therapeutic agents for thermo-chemotherapy treatment of cancer, *Nanoscale*, 2010, **6**, 11573.

19 M. Iranmanesh and J. Hulliger, Magnetic separation: its application in mining, waste purification, medicine, biochemistry and chemistry, *Chem. Soc. Rev.*, 2017, **46**, 5925–5934.

20 L. Liu, Y. Ma, X. Chen, X. Xiong and S. Shi, Screening and identification of BSA bound ligands from Puerariae lobata flower by BSA functionalized Fe_3O_4 magnetic nanoparticles coupled with HPLC-MS/MS, *J. Chromatogr. B: Anal. Technol. Biomed. Life Sci.*, 2012, **887–888**, 55–60.

21 D. T. Ta, R. Vanella and M. A. Nash, Magnetic Separation of Elastin-like Polypeptide Receptors for Enrichment of Cellular and Molecular Targets, *Nano Lett.*, 2017, **17**, 7932–7939.

22 A. I. Goncalves, M. S. Miranda, M. T. Rodrigues, R. L. Reis and M. E. Gomes, Magnetic responsive cell-based strategies for diagnostics and therapeutics, *Biomed. Mater.*, 2018, **13**, 054001.

23 H. Bi and X. Han, Magnetic field triggered drug release from lipid microcapsule containing lipid-coated magnetic nanoparticles, *Chem. Phys. Lett.*, 2018, **706**, 455–460.

24 S. Dutta, S. Parida, C. Maiti, R. Banerjee, M. Mandal and D. Dhara, Polymer grafted magnetic nanoparticles for delivery of anticancer drug at lower pH and elevated temperature, *J. Colloid Interface Sci.*, 2016, **467**, 70–80.

25 X. Guo, W. Li, L. Luo, Z. Wang, Q. Li, F. Kong, H. Zhang, J. Yang, C. Zhu, Y. Du and J. You, External Magnetic Field-Enhanced Chemo-Photothermal Combination Tumor Therapy via Iron Oxide Nanoparticles, *ACS Appl. Mater. Interfaces*, 2017, **9**, 16581–16593.

26 A. C. Silva, T. R. Oliveira, J. B. Mamani, S. M. Malheiros, L. Malavolta, L. F. Pavon, T. T. Sibov, E. Amaro Jr, A. Tannus, E. L. Vidoto, M. J. Martins, R. S. Santos and L. F. Gamarra, Application of hyperthermia induced by superparamagnetic iron oxide nanoparticles in glioma treatment, *Int. J. Nanomed.*, 2011, **6**, 591–603.

27 J. M. Shen, X. X. Li, L. L. Fan, X. Zhou, J. M. Han, M. K. Jia, L. F. Wu, X. X. Zhang and J. Chen, Heterogeneous dimer peptide-conjugated polylysine dendrimer-Fe_3O_4 composite as a novel nanoscale molecular probe for early diagnosis and therapy in hepatocellular carcinoma, *Int. J. Nanomed.*, 2017, **12**, 1183–1200.

28 Y. Li, W. Shang, X. Liang, C. Zeng, M. Liu, S. Wang, H. Li and J. Tian, The diagnosis of hepatic fibrosis by magnetic resonance and near-infrared imaging using dual-modality nanoparticles, *RSC Adv.*, 2018, **8**, 6699–6708.

29 N. Mahmed, O. Heczko, A. Lancok and S. P. Hannula, The magnetic and oxidation behavior of bare and silica-coated iron oxide nanoparticles synthesized by reverse co-precipitation of ferrous ion (Fe^{2+}) in ambient atmosphere, *J. Magn. Magn. Mater.*, 2014, **353**, 15–22.

30 W. J. Yang, J. H. Lee, S. C. Hong, J. Lee, J. Lee and D. W. Han, Difference between Toxicities of Iron Oxide Magnetic Nanoparticles with Various Surface-Functional Groups against Human Normal Fibroblasts and Fibrosarcoma Cells, *Materials*, 2013, **6**, 4689–4706.

31 S. Karthi, G. A. Kumar, D. K. Sardar, G. C. Dannangoda, K. S. Martirosyan and E. K. Girija, Fluorapatite coated iron oxide nanostructure for biomedical applications, *Mater. Chem. Phys.*, 2017, **193**, 356–363.

32 J. Lee, S. Zhang and S. Sun, High-Temperature Solution-Phase Syntheses of Metal-Oxide Nanocrystals, *Chem. Mater.*, 2013, **25**, 1293–1304.

33 J. Cai, Y. Q. Miao, B. Z. Yu, P. Ma, L. Li and H. M. Fan, Large-Scale, Facile Transfer of Oleic Acid-Stabilized Iron Oxide Nanoparticles to the Aqueous Phase for Biological Applications, *Langmuir*, 2017, **33**, 1662–1669.

34 S. Kurzhals, N. Gal, R. Zirbs and E. Reimhult, Controlled aggregation and cell uptake of thermoresponsive polyoxazoline-grafted superparamagnetic iron oxide nanoparticles, *Nanoscale*, 2017, **9**, 2793–2805.

35 B. Wang, F. Zhang, Q. Jianhua, Z. Xuehong, C. Hong, Y. Du and P. Xu, Preparation of Fe_3O_4 superparamagnetic nanocrystals by coprecipitation with ultrasonic enhancement and their characterization, *Acta Chim. Sin.*, 2009, **67**, 1211–1216.

36 J. Mürbe, A. Rechtenbach and J. Töpfer, Synthesis and physical characterization of magnetite nanoparticles for biomedical applications, *Mater. Chem. Phys.*, 2008, **110**, 426–433.

37 S. F. Oliveira, G. Bisker, N. A. Bakh, S. L. Gibbs, M. P. Landry and M. S. Strano, Protein functionalized carbon nanomaterials for biomedical applications, *Carbon*, 2015, **95**, 767–779.

38 X. Cui, S. Xu, X. Wang and C. Chen, The nano-bio interaction and biomedical applications of carbon nanomaterials, *Carbon*, 2018, **138**, 436–450.

39 N. L. Teradal and R. Jelinek, Carbon Nanomaterials in Biological Studies and Biomedicine, *Adv. Healthcare Mater.*, 2017, **6**, 1700574.

40 C. He, S. Wu, N. Zhao, C. Shi, E. Liu and J. Li, Carbon-Encapsulated Fe_3O_4 Nanoparticles as a High-Rate Lithium Ion Battery Anode Material, *ACS Nano*, 2013, **7**, 4459–4469.

41 N. Zhao, S. Wu, C. He, Z. Wang, C. Shi, E. Liu and J. Li, One-pot synthesis of uniform Fe_3O_4 nanocrystals encapsulated in interconnected carbon nanospheres for superior lithium storage capability, *Carbon*, 2013, **57**, 130–138.

42 L. Kong, X. Lu, X. Bian, W. Zhang and C. Wang, Constructing carbon-coated Fe_3O_4 microspheres as antiacid and magnetic support for palladium nanoparticles for catalytic applications, *ACS Appl. Mater. Interfaces*, 2011, **3**, 35–42.

43 J. Zhang, K. Wang, Q. Xu, Y. Zhou, F. Cheng and S. Guo, Beyond Yolk-Shell Nanoparticles:$Fe_3O_4@Fe_3C$ Core@Shell Nanoparticles as Yolks and Carbon Nanospindles as Shells for Efficient Lithium Ion Storage, *ACS Nano*, 2015, **9**, 3369–3376.

44 W.-M. Zhang, X.-L. Wu, J.-S. Hu, Y.-G. Guo and L.-J. Wan, Carbon Coated Fe_3O_4 Nanospindles as a Superior Anode Material for Lithium-Ion Batteries, *Adv. Funct. Mater.*, 2008, **18**, 3941–3946.

45 L. Wang, K. Lin, J. Ren, K. Du, Y. Chang, L. Han, P. Yao and F. Tian, Direct synthesis of ultrasmall and stable magnetite nanoparticles coated with one single carbon layer for sensitive surface-enhanced Raman scattering, *Appl. Surf. Sci.*, 2019, **478**, 601–606.

46 A. Abdolmaleki, S. Mallakpour, M. Mahmoudian and M. R. Sabzalian, A new polyamide adjusted triazinyl-β-cyclodextrin side group embedded magnetic nanoparticles for bacterial capture, *Chem. Eng. J.*, 2017, **309**, 321–329.

47 K. Lin, L. Wang, F. Tian, K. Du, Y. Chang, L. Han and P. Yao, A facile and controllable protocol for simultaneous synthesis of magnetite nanoparticles and luminescent carbon dots, *J. Alloys Compd.*, 2018, **769**, 360–366.

48 O. N. Shebanova and P. Lazor, Raman spectroscopic study of magnetite ($FeFe_2O_4$): a new assignment for the vibrational spectrum, *Solid State Chem.*, 2003, **174**, 424–430.

49 A. C. Ferrari, J. C. Meyer, V. Scardaci, C. Casiraghi, M. Lazzeri, F. Mauri, S. Piscanec, D. Jiang, K. S. Novoselov, S. Roth and A. K. Geim, Raman spectrum of graphene and graphene layers, *Phys. Rev. Lett.*, 2006, **97**, 187401.

50 W. Shen, X. Lin, C. Jiang, C. Li, H. Lin, J. Huang, S. Wang, G. Liu, X. Yan, Q. Zhong and B. Ren, Reliable Quantitative SERS Analysis Facilitated by Core-Shell Nanoparticles with Embedded Internal Standards, *Angew. Chem., Int. Ed. Engl.*, 2015, **54**, 7308–7312.

51 Q. An, P. Zhang, J. M. Li, W. F. Ma, J. Guo, J. Hu and C. C. Wang, Silver-coated magnetite-carbon core-shell microspheres as substrate-enhanced SERS probes for detection of trace persistent organic pollutants, *Nanoscale*, 2012, **4**, 5210–5216.

52 D. Song, R. Yang, C. Wang, R. Xiao and F. Long, Reusable nanosilver-coated magnetic particles for ultrasensitive SERS-based detection of malachite green in water samples, *Sci. Rep.*, 2016, **6**, 22870.

53 H. Wang, Q.-W. Chen, Y.-F. Yu, K. Cheng and Y.-B. Sun, Size- and Solvent-Dependent Magnetically Responsive Optical Diffraction of Carbon-Encapsulated Superparamagnetic Colloidal Photonic Crystals, *J. Phys. Chem. C*, 2011, **115**, 11427–11434.

54 R. Frison, G. Cernuto, A. Cervellino, O. Zaharko, G. M. Colonna, A. Guagliardi and N. Masciocchi, Magnetite–Maghemite Nanoparticles in the 5–15 nm Range: Correlating the Core–Shell Composition and the Surface Structure to the Magnetic Properties. A Total Scattering Study, *Chem. Mater.*, 2013, **25**, 4820–4827.

55 X. Li, Y. Liu, X. Song, H. Wang, H. Gu and H. Zeng, Intercrossed carbon nanorings with pure surface states as low-cost and environment-friendly phosphors for white-light-emitting diodes, *Angew. Chem., Int. Ed. Engl.*, 2015, **54**, 1759–1764.

56 H. Fatima, D.-W. Lee, H. J. Yun and K.-S. Kim, Shape-controlled synthesis of magnetic Fe_3O_4 nanoparticles with different iron precursors and capping agents, *RSC Adv.*, 2018, **8**, 22917–22923.

57 X. Zhou, G. Zhao and Y. Liu, Uniform hollow magnetite spheres: facile synthesis, growth mechanism, and their magnetic properties, *Mater. Res. Bull.*, 2014, **59**, 358–364.

58 R. Rajendran, R. Muralidharan, R. Santhana Gopalakrishnan, M. Chellamuthu, S. U. Ponnusamy and E. Manikandan, Controllable Synthesis of Single-Crystalline Fe_3O_4 Nanorice by a One-Pot, Surfactant-Assisted Hydrothermal Method and Its Properties, *Eur. J. Inorg. Chem.*, 2011, 5384–5389.

59 Z. R. Xu, W. Zhu and S. H. Htar, Partial oxidative gasification of municipal sludge in subcritical and supercritical water, *Environ. Technol.*, 2012, **33**, 1217–1223.

60 H. Yang, H. Hu, Z. Ni, C. K. Poh, C. Cong, J. Lin and T. Yu, Comparison of surface-enhanced Raman scattering on graphene oxide, reduced graphene oxide and graphene surfaces, *Carbon*, 2013, **62**, 422–429.

61 W. Xu, N. Mao and J. Zhang, Graphene: a platform for surface-enhanced Raman spectroscopy, *Small*, 2013, **9**, 1206–1224.

62 X. Ling and J. Zhang, Interference Phenomenon in Graphene-Enhanced Raman Scattering, *J. Phys. Chem. C*, 2011, **115**, 2835–2840.

63 S. Chen, X. Li, Y. Zhao, L. Chang and J. Qi, Graphene oxide shell-isolated Ag nanoparticles for surface-enhanced Raman scattering, *Carbon*, 2015, **81**, 767–772.

64 J. Shen, Y. Zhu, X. Yang, J. Zong and C. Li, Multifunctional Fe_3O_4@Ag/SiO_2/Au core-shell microspheres as a novel SERS-activity label via long-range plasmon coupling, *Langmuir*, 2013, **29**, 690–695.

65 C. J. Orendorff, A. Gole, T. K. Sau and C. J. Murphy, Surface-Enhanced Raman Spectroscopy of Self-Assembled Monolayers: Sandwich Architecture and Nanoparticle Shape Dependence, *Anal. Chem.*, 2005, **77**, 3261–3266.

66 B. Li, H.-H. Wu, P.-F. Luo, K. Lin, J.-G. Cheng, H.-H. Zhong, Y. Jiang and Y.-W. Lu, Size-Dependent Plasmonic Mode Evolution and SERS Performance of β-Sn Nanoparticles, *J. Phys. Chem. C*, 2018, **123**, 735–738.

67 Y. H. Ngo, D. Li, G. P. Simon and G. Garnier, Gold nanoparticle-paper as a three-dimensional surface enhanced Raman scattering substrate, *Langmuir*, 2012, **28**, 8782–8790.